PHYSICAL REVIEW D **100,** 124046 (2019)

# Constructing binary neutron star initial data with high spins, high compactnesses, and high mass ratios

Wolfgang Tichy,[1] Alireza Rashti,[1] Tim Dietrich,[2] Reetika Dudi,[3,4] and Bernd Brügmann[4]
[1]*Department of Physics, Florida Atlantic University, Boca Raton, Florida 33431, USA*
[2]*Nikhef, Science Park 105, 1098 XG Amsterdam, The Netherlands*
[3]*Max Planck Institute for Gravitational Physics (Albert Einstein Institute), Am Mühlenberg 1, Potsdam 14476, Germany*
[4]*Theoretical Physics Institute, University of Jena, 07743 Jena, Germany*

(Received 24 October 2019; published 18 December 2019)

The construction of accurate and consistent initial data for various binary parameters is a critical ingredient for numerical relativity simulations of the compact binary coalescence. In this article, we present an upgrade of the pseudospectral SGRID code, which enables us to access even larger regions of the binary neutron star parameter space. As a proof of principle, we present a selected set of first simulations based on initial configurations computed with the new code version. In particular, we simulate two millisecond pulsars close to their breakup spin, highly compact neutron stars with masses at about 98% of the maximum supported mass of the employed equation of state, and unequal-mass systems with mass ratios even outside the range predicted by population synthesis models ($q = 2.03$). The discussed code extension will help us to simulate previously unexplored binary configurations. This is a necessary step to construct and test new gravitational-wave approximants and to interpret upcoming binary neutron star merger observations. When we construct initial data, we have to specify various parameters, such as a rotation parameter for each star. Some of these parameters do not have direct physical meaning, which makes comparisons with other methods or models difficult. To facilitate this, we introduce simple estimates for the initial spin, momentum, mass, and center of mass (c.m.) of each individual star.

DOI: 10.1103/PhysRevD.100.124046

## I. INTRODUCTION

In August 2017, the combined detection of a gravitational-wave (GW) signal and the detection of electromagnetic (EM) signals across the whole spectrum emitted from the same astrophysical source, very likely a binary neutron star (BNS) merger [1], initiated a new era of multimessenger astronomy [7,8].

While there are analytical models to describe BNS coalescence as long as the two stars are well separated, the highly nonlinear regime around the moment of merger is only accessible with full numerical relativity (NR) simulations. These simulations allow us to study the dynamics, GW signal, and possible EM counterparts, and are therefore required for a true multimessenger interpretation.

Most NR simulations are based on a $3 + 1$ decomposition in which four-dimensional spacetime is foliated by spacelike hypersurfaces. This means that for a successful numerical simulation one has to solve the Einstein equations and the equations governing general-relativistic matter on a spacelike hypersurface as an initial condition; see, e.g., Ref. [9] or Ref. [10] and references therein. Generally, these initial data have to provide configurations in which the stars are sufficiently far away from each other to allow a study of the emitted GW signal, but one also wants a distance short enough to avoid the computational cost of too many orbits. Current state-of-the-art BNS simulations reach from a few orbits up to 22 orbits prior to merger [11].

Given the diversity of the BNS population, one has to be able to construct accurate initial data for a variety of different binary parameters for an accurate interpretation of future detections. As an example, even relatively small spins can, if neglected, lead to biases in the estimation of the source properties (e.g., Refs. [12–14]). This fact together with the observation of a number of highly spinning neutron stars (NSs) [e.g., PSR J1748–2446ad [15] (the fastest spinning NS, 716 Hz), PSR J1807-2500B [16] (the fastest spinning NS in a binary, 239 Hz), and PSR J1946 + 2052 [17] (the fastest spinning NS in a BNS system, 59 Hz)] make the accurate modeling of spin effects indispensable.

Similarly, the observation of massive NSs with $m_{\mathrm{NS}} > 2\,M_\odot$ (e.g., PSR J0740 + 6620 [18] with $m = 2.14^{+0.10}_{-0.09}$) shows that it is important to simulate stars with high masses and thus high compactnesses. Collisions of such massive stars might be almost indistinguishable from the merger of small black holes (BHs), since the amount of ejected material and consequently the brightness of the kilonova typically decrease for high compactnesses and larger total masses [19,20], and since tidal effects become too small to be reliably measured during the inspiral [21,22]. Additional simulations are needed to further improve estimates of the prompt collapse threshold [23,24], i.e., the mass at which the colliding neutron stars immediately form a black hole. Such threshold mass estimates, in addition to a detailed understanding of when and which EM signals might be observable before the merger [25,26], will become important once the increasing number of GW triggers make expensive EM follow-up campaigns for all potential GW candidates very difficult [27]. This can be used to reduce observational overhead.

Finally, as shown in, e.g., Refs. [19,28–32], the mass ratio of a BNS system affects the GW and EM signals, where higher-mass-ratio systems are typically less GW- but more EM-bright. Based on the distribution of isolated, observed NSs, mass ratios up to $q_{\max} \simeq 2.3$ are allowed, contrary to population synthesis models which predict maximal values of $q_{\max} \simeq 1.8$–$1.9$ (e.g., Refs. [33,34]). To date, a maximum mass ratio of only $q \sim 1.3$ [35,36] has been observationally confirmed; however, this small value might purely be a selection effect due to the limited number of observed BNS systems with well-constrained individual masses.

Over the years, the numerical relativity community has developed a number of codes for computing BNS initial data in certain portions of the parameter space. Some of the best-known codes are the open source spectral code LORENE [37] with nonpublic extensions (e.g., Ref. [38]), the Princeton group's multigrid solver [39], BAM's multigrid solver [40,41], the COCAL code [42,43], SpEC's spectral solver Spells [44,45], and the spectral code SGRID [34,46–48]. Recent developments include Refs. [49,50].

These codes have been employed for a variety of studies in different corners of BNS parameter space [51], such as spinning BNSs [29,34,52–56], precessing BNSs [34,45,57], eccentricity-reduced BNSs [11,53,58–63], highly eccentric BNSs [64], high-mass BNSs (e.g., Refs. [24,32,65,66]), and high-mass-ratio systems [34,67].

Despite these advances, there are a number of possible configurations which, so far, have been out of reach for the NR community, e.g., configurations with total masses above $M \sim 3.4\ M_\odot$ have, to our knowledge, not been simulated before. Similarly, highly spinning and precessing systems close to the breakup or high-mass-ratio systems for soft equations of state (EoSs) have been out of reach for the numerical relativity community. All of these configurations are not excluded by population synthesis models (e.g., Ref. [33]) and therefore should be studied. Even more importantly, extreme corners of the parameter space have to be covered properly to be able to test the reliability of waveform approximants in regions in which they are employed during the analysis of GW signals; see, e.g., Refs. [7,21,68,69].

Thus, to be prepared for future BNS mergers, we have upgraded our initial data code SGRID to allow a computation of BNS systems for large spins, compactnesses, and mass ratios. As a proof of principle, we present the first dynamical simulation of a BNS merger of two neutron stars close to the breakup spin, a simulation with the highest mass ratio ($q = 2.03$) considered in numerical relativity for a soft equation of state, and a simulation with two stars which have 98% of the maximum allowed mass for the employed EoS. In addition, all of these simulations employ eccentricity-reduced initial data, which is an important ingredient for the production of high-quality data.

The article is structured as follows. Section II gives an overview of the equations which we need to solve to obtain consistent initial configurations. Section III summarizes the numerical methods employed in the upgraded SGRID code. In Sec. V we present the results for particular initial data, and in Sec. VI we perform preliminary simulations to prove the robustness of our new methods. We conclude in Sec. VII. In addition, we present an empirical relation between the NS spin and SGRID's input parameters, the employed procedure for the eccentricity reduction, and a comparison between the old and new SGRID codes in the Appendices.

Throughout the article, we use geometric units in which $G = c = 1$, as well as $M_\odot = 1$. Latin indices such as $i$ run from 1 to 3 and denote spatial indices, while greek indices such as $\mu$ run from 0 to 3 and denote spacetime indices.

## II. BINARY NEUTRON STARS WITH SPIN IN QUASIEQUILIBRIUM

We start by briefly describing the equations governing BNSs in arbitrary rotation states in general relativity. These equations were derived in Refs. [70,71] and extended to the case of eccentric orbits in Refs. [34,40]; see also Ref. [72] for a possible generalization. We refer to the review in Ref. [10] for further references.

We base our method on the Arnowitt-Deser-Misner (ADM) decomposition of the Einstein equations [73] and rewrite the 4-metric $g_{\mu\nu}$ in terms of the 3-metric $\gamma_{ij}$, the lapse $\alpha$, the shift $\beta^i$, and the extrinsic curvature $K^{ij}$. The NS matter is assumed to be a perfect fluid with stress-energy tensor

$$T^{\mu\nu} = [\rho_0(1+\epsilon) + P]u^\mu u^\nu + P g^{\mu\nu}. \qquad (1)$$

Here $\rho_0$ is the rest-mass density (which is proportional to the number density of baryons), $P$ is the pressure, $\epsilon$ is the internal energy density divided by $\rho_0$, and $u^\mu$ is the 4-velocity of the fluid. We also introduce the specific enthalpy

$$h = 1 + \epsilon + P/\rho_0. \qquad (2)$$

This quantity is useful because if we assume a polytropic equation of state

$$P = \kappa \rho_0^{1+1/n}, \tag{3}$$

we can express the rest-mass density, the pressure, and the internal energy in terms of it. The $n$ here is known as the polytropic index, and $\kappa$ is a constant. In this paper we consider several different EoSs, all approximated by piecewise polytropes following Ref. [74]. Each piece is defined within a certain interval in $\rho_0$ and has its own $n_i$ and $\kappa_i$ in this interval. Within each polytrope piece we find

$$\begin{aligned} \rho_0 &= \kappa_i^{-n_i}\left(\frac{h-k_i}{n_i+1}\right)^{n_i}, \\ P &= \kappa_i^{-n_i}\left(\frac{h-k_i}{n_i+1}\right)^{n_i+1}, \\ \epsilon &= \frac{n_i}{n_i+1}(h-1) + \frac{k_i-1}{n_i+1}. \end{aligned} \tag{4}$$

The constants $n_i$, $\kappa_i$, and $k_i$ have to be chosen such that $P$ and $\epsilon$ are continuous across the $\rho_0$ intervals. For the $\rho_0$ interval starting at $\rho_0 = 0$, which corresponds to the outermost layer of the star, one obtains $k = 0$.

We express the fluid 4-velocity $u^\mu$ in terms of the 3-velocity

$${}^{(3)}\tilde{u}^i = h\gamma^i_\nu u^\nu, \tag{5}$$

which in turn is split into an irrotational piece $D^i\phi$ and a rotational piece $w^i$,

$${}^{(3)}\tilde{u}^i = D^i\phi + w^i, \tag{6}$$

where $D_i$ is the derivative operator compatible with the 3-metric $\gamma_{ij}$.

In order to simplify the problem and obtain elliptic equations, we make several assumptions. The first is the existence of an approximate symmetry vector $\xi^\mu$, such that

$$\pounds_\xi g_{\mu\nu} \approx 0. \tag{7}$$

We also assume similar equations for scalar matter quantities such as $h$. For a spinning star, however, $\pounds_\xi u^\mu$ is nonzero. Instead, we assume that

$$\gamma^\nu_i \pounds_\xi (\nabla_\nu \phi) \approx 0, \tag{8}$$

so that the time derivative of the irrotational piece of the fluid velocity vanishes in corotating coordinates. We also assume that

$$\gamma^\nu_i \pounds_{\frac{\nabla\phi}{hu^0}} w_\nu \approx 0, \tag{9}$$

and

$${}^{(3)}\pounds_{\frac{w}{hu^0}} w_i \approx 0, \tag{10}$$

which describe the fact that the rotational piece of the fluid velocity is constant along the world line of the star center.

These approximations together with the additional assumptions of maximal slicing

$$\gamma_{ij}K^{ij} = 0 \tag{11}$$

and conformal flatness

$$\gamma_{ij} = \psi^4 \delta_{ij} \tag{12}$$

yield the following coupled equations:

$$\bar{D}^2\psi + \frac{\psi^5}{32\alpha^2}(\bar{L}B)^{ij}(\bar{L}B)_{ij} + 2\pi\psi^5\rho = 0, \tag{13}$$

$$\bar{D}_j(\bar{L}B)^{ij} - (\bar{L}B)^{ij}\bar{D}_j \ln(\alpha\psi^{-6}) - 16\pi\alpha\psi^4 j^i = 0, \tag{14}$$

$$\bar{D}^2(\alpha\psi) - \alpha\psi\left[\frac{7\psi^4}{32\alpha^2}(\bar{L}B)^{ij}(\bar{L}B)_{ij} + 2\pi\psi^4(\rho + 2S)\right] = 0, \tag{15}$$

$$D_i\left[\frac{\rho_0\alpha}{h}(D^i\phi + w^i) - \rho_0\alpha u^0(\beta^i + \xi^i)\right] = 0, \tag{16}$$

and

$$h = \sqrt{L^2 - (D_i\phi + w_i)(D^i\phi + w^i)}. \tag{17}$$

Here $(\bar{L}B)^{ij} = \bar{D}^i B^j + \bar{D}^j B^i - \frac{2}{3}\delta^{ij}\bar{D}_k B^k$, $\bar{D}_i = \partial_i$, and we have introduced

$$B^i = \beta^i + \xi^i + \Omega\epsilon^{ij3}(x^j - x^j_{CM}), \tag{18}$$

$$\begin{aligned} \rho &= \alpha^2[\rho_0(1+\epsilon) + P]u^0u^0 - P, \\ j^i &= \alpha[\rho_0(1+\epsilon) + P]u^0u^0(u^i/u^0 + \beta^i), \\ S^{ij} &= [\rho_0(1+\epsilon) + P]u^0u^0(u^i/u^0 + \beta^i)(u^j/u^0 + \beta^j) \\ &\quad + P\gamma^{ij}, \end{aligned} \tag{19}$$

$$\begin{aligned} u^0 &= \frac{\sqrt{h^2 + (D_i\phi + w_i)(D^i\phi + w^i)}}{\alpha h}, \\ L^2 &= \frac{b + \sqrt{b^2 - 4\alpha^4[(D_i\phi + w_i)w^i]^2}}{2\alpha^2}, \\ b &= [(\xi^i + \beta^i)D_i\phi - C]^2 + 2\alpha^2(D_i\phi + w_i)w^i, \end{aligned} \tag{20}$$

where we sum over repeated spatial indices, and $C$ is a constant of integration that, in general, can have a different value inside each star.

In addition to the construction of BNS configurations with arbitrary spin, we also want to vary the eccentricity of the systems. Thus, we follow the methods that we developed in Ref. [40] (see also Ref. [10]). In this approach, the symmetry vector has the form

$$\begin{aligned} \xi^0_{1/2} &= 1, \\ \xi^i_{1/2} &= \Omega(-x^2, x^1 - x^1_{c1/2}, 0) + \frac{v_r}{r_{12}}(x^i - x^i_{CM}), \end{aligned} \tag{21}$$

where $\Omega$ is the orbital angular velocity chosen to lie along the $x^3$ direction and $v_r$ is the radial velocity that needs to be negative for a true inspiral. Here, $x^i_{CM}$ denotes the c.m. position of the system, $r_{12}$ is the distance between the two star centers, and

$$x^1_{c1/2} = x^1_{CM} + e(x^1_{C*1/2} - x^1_{CM}) \tag{22}$$

depends on the eccentricity parameter $e$ and the location of the two star centers $x^1_{C*1/2}$. The specific form of Eq. (21) is derived from the following two assumptions: (i) $\xi^\mu$ is along the motion of the star center, and (ii) without inspiral, each star center moves along a segment of an elliptic orbit at apoapsis that can be approximated by its inscribed circle. The eccentricity parameter $e$ that appears in $x^1_{c1/2}$ and the radial velocity $v_r$ are freely adjustable to obtain any orbit we want. Using this new symmetry vector $\vec{\xi}_{1/2}$, we can still solve the initial data equations with the same methods as described before. Most importantly, in order to obtain a true inspiral orbit with low eccentricity, we can adjust both $e$ and $v_r$, while $\Omega$ can be adjusted by other means such as the "force balance" method discussed below. Or, we can set $e = 0$ and directly adjust $\Omega$ and $v_r$, as discussed in Appendix B.

The elliptic equations (13), (14), (15), and (16) have to be solved by incorporating the boundary conditions

$$\lim_{r\to\infty}\psi = 1, \qquad \lim_{r\to\infty}B^i = 0, \qquad \lim_{r\to\infty}\alpha\psi = 1 \tag{23}$$

at spatial infinity and

$$(D^i\phi)D_i\rho_0 + w^i D_i\rho_0 = hu^0(\beta^i + \xi^i)D_i\rho_0 \tag{24}$$

at each star's surface. While, in general, the rotational piece of the fluid velocity $w^i$ can be chosen freely, we will use the form

$$w^i = \epsilon^{ijk}\omega^j(x^k - x^k_{C*}), \tag{25}$$

which (as demonstrated in Ref. [71]) results in almost rigidly rotating fluid configurations with low expansion and shear. The parameter $x^k_{C*}$ denotes the location of the star center and $\omega^j$ is an arbitrarily chosen vector that determines the star's spin. Summation over the repeated indices $j$ and $k$ is implied.

Once the equations (13), (14), (15), (16), and (17) are solved, we know $h$ (and thus the matter distribution) and the fluid 3-velocity ${}^{(3)}\tilde{u}^i$ via Eq. (6). The 3-metric is obtained from Eq. (12) and the extrinsic curvature is given by

$$K^{ij} = \frac{1}{2\psi^4\alpha}(\bar{L}\beta)^{ij}. \tag{26}$$

## III. NUMERICAL METHOD

The elliptic equations (13), (14), (15), and (16) together with the algebraic equation (17) are the main equations that we have to solve in order to construct initial data. We do so using the SGRID program [34,46–48], which uses pseudospectral methods to accurately compute spatial derivatives. We will solve the whole set of equations using an iterative procedure, where we first solve the elliptic equations for a given matter distribution $h$, then update the matter using the algebraic equation (17), and then go back to the first step.

### A. Surface fitting coordinates

The matter inside each star is smooth. However, at the surface (at $h = 1$), $\rho_0$, $P$, and $\epsilon$ are not differentiable. So if we want to take full advantage of a spectral method, the star surfaces should be domain boundaries. However, when we update the matter distribution given by $h$ within our iterative approach the stars change shape. Hence, the domain boundaries have to be adjusted as well. In order to address this problem we cover space by multiple domains, each described by their own coordinates. For the star domains these coordinates depend on a freely specifiable function which will allow us to adapt the domain boundaries to the star surface. In the past we have done this by making use of the coordinates $(A, B, \varphi)$ introduced by Ansorg [75], which can cover all of space using only six computational domains. Here the coordinates $A$ and $B$ both range from 0 to 1, and $\varphi$ is a polar angle measured around the $x$ axis. The coordinate transformations contain freely specifiable functions $\sigma_\pm(B, \varphi)$ that can be chosen such that domain boundaries coincide with the star surfaces. Unfortunately, the coordinate transformation from Ansorg coordinates $(A, B, \varphi)$ to Cartesian-like coordinates $(x, y, z)$ is so complicated that its inverse cannot be written down analytically. This makes it hard to adjust the functions $\sigma_\pm$ so that domain boundaries coincide with the star surfaces, and has to be tackled with an extra numerical root finder. Furthermore, the coordinate transformation is also singular in certain regions. When we solve elliptic equations with a Newton scheme we have to solve a linear problem for each Newton step. However, the condition numbers of the matrices describing this linear problem are very high due to the coordinate singularities mentioned

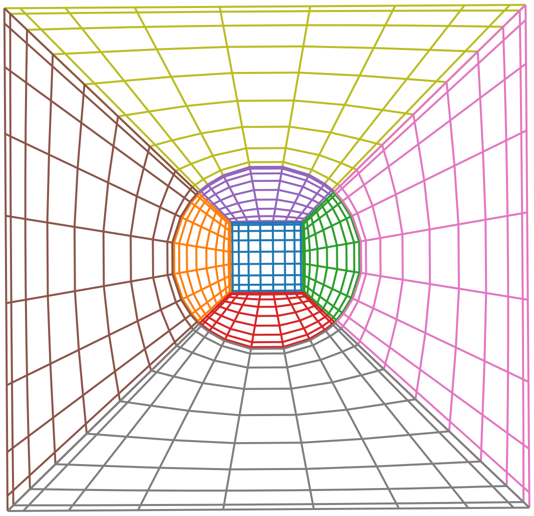

FIG. 1. Some domains and their coordinate lines in the $xy$ plane. Plotted are the domains inside and around neutron star 1. The star is roughly spherical and covered by a central cube and six cubed sphere wedges, four of which are shown because they intersect the $xy$ plane. The space around the star is covered by six more domains to form a larger cube.

before. This can lead to numerical inaccuracies that are hard to deal with.

For these reasons we have modified SGRID so that we can now use surface fitting cubed sphere coordinates $(\lambda, A, B)$ that have no singularities anywhere. In Fig. 1 we show the coordinate lines in the $z = 0$ plane. The star is covered by a central cube surrounded by several cubed sphere wedges. The space around the star is covered by several more domains. All domains together cover a larger cube containing the star and its surroundings. The coordinate transformation for the green wedge covering the star interior to the right of the central cube is given by

$$\begin{aligned} x &= x_{C*} + (a_1 - a_0)\lambda + a_0, \\ y &= y_{C*} + [(a_1 - a_0)\lambda + a_0]A, \\ z &= z_{C*} + [(a_1 - a_0)\lambda + a_0]B, \end{aligned} \tag{27}$$

where $\lambda \in [0, 1]$, $A, B \in [-1, 1]$ and

$$a_1 = \frac{\sigma_1(A, B)}{\sqrt{1 + A^2 + B^2}}, \qquad a_0 = \text{const}. \tag{28}$$

The function $\sigma_1(A, B)$ determines the shape of the star surface. Notice that for $\sigma_1(A, B) = R_* = \text{const}$ we obtain a spherical star surface with radius $R_*$. The coordinate lines in Fig. 1 are obtained for $B = 0$. The coordinate transformation for the other wedges inside the star can be obtained by exchanging $x$ with $y$ or $z$ and by possible sign changes of $a_1$ and $a_0$. For example, the red wedge covering the star interior below the central cube is given by

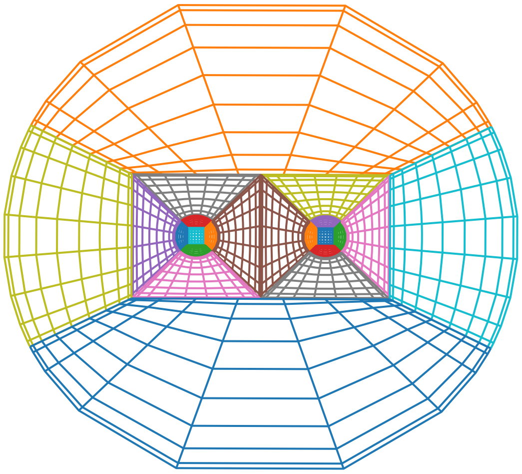

FIG. 2. The domains in and around both stars augmented by several more domains. The result is a large sphere that covers both stars and their surroundings.

$$\begin{aligned} y &= y_{C*} + (a_1 - a_0)\lambda + a_0, \\ x &= x_{C*} + [(a_1 - a_0)\lambda + a_0]A, \\ z &= z_{C*} + [(a_1 - a_0)\lambda + a_0]B, \end{aligned} \tag{29}$$

where now

$$a_1 = -\frac{\sigma_1(A, B)}{\sqrt{1 + A^2 + B^2}}, \qquad a_0 = -\text{const}. \tag{30}$$

The inverted wedges just outside the stars are obtained by reversing the roles of $a_1$ and $a_0$. For the domain just below the red wedge we would have

$$a_0 = -\frac{\sigma_1(A, B)}{\sqrt{1 + A^2 + B^2}}, \qquad a_1 = -\text{const}, \tag{31}$$

while still using Eq. (29).

Figure 2 shows how two such larger cubes as in Fig. 1 can be put next to each other, and in turn be surrounded by more wedges so as to cover a large sphere. This sphere can in turn be surrounded by shells that can be obtained by choosing

$$a_0 = \frac{\sigma_{\text{in}}}{\sqrt{1 + A^2 + B^2}}, \qquad a_1 = \frac{\sigma_{\text{out}}}{\sqrt{1 + A^2 + B^2}}, \tag{32}$$

where $\sigma_{\text{in}}$ and $\sigma_{\text{out}}$ denote the inner and outer radius of the shell. Since we have to impose the boundary conditions of Eq. (23) at infinity one should choose $\sigma_{\text{out}}$ to be very large. However, for a given number of grid points in $\lambda$ this will result in poor resolution in the radial direction, which could adversely affect the accuracy of our method. For this reason we introduce yet another coordinate transformation. If we define $r \coloneqq \sqrt{x^2 + y^2 + z^2}$ and $L \coloneqq \sigma_{\text{out}} - \sigma_{\text{in}}$, then Eqs. (27) and (32) result in

$$r = L\lambda + \sigma_{\rm in}. \tag{33}$$

So if we want a domain that extends to a large radius it is advantageous to replace the $\lambda$ coordinate with

$$\rho = \frac{\sigma_{\rm out}}{L}\left(1 - \frac{\sigma_{\rm in}}{r}\right) = \frac{\sigma_{\rm out}}{L}\left(1 - \frac{\sigma_{\rm in}}{L\lambda + \sigma_{\rm in}}\right). \tag{34}$$

Then, a quantity $\Psi$ that behaves as $\Psi \sim b_1 + b_2/r$ for large $r$ becomes $\Psi \sim c_1 + c_2\rho$, when expressed in terms of $\rho$ (here $b_1$, $b_2$, $c_1$, and $c_2$ are constants). Thus, if within our spectral method we expand $\Psi(\rho)$ in terms of Chebyshev polynomials only the first few coefficients will be non-negligible, which leads to a very good approximation when we keep only a finite number of terms. This would not be the case if we used $\lambda$ as our coordinate since then $\Psi \sim d_1 + d_2/\lambda$, which is not a polynomial in $\lambda$.

### B. Nonlinear equations that we have to solve

In order to construct initial data we have to solve the elliptic equations (13), (14), (15), and (16). This is done using SGRID's pseudospectral method (as in Refs. [46–48]), where we use Chebyshev expansions and introduce grid points at the Chebyshev extrema. Once the number of grid points is chosen all derivatives are approximated by certain linear combinations of the field values at the grid points. Such a pseudospectral method is similar in spirit to finite differences but it uses all grid points in one direction to approximate a derivative in this direction, and thus is much more accurate for smooth fields. Once all derivatives have been discretized in this way, we end up with a set of nonlinear equations for all fields at all grid points. This system of equations has the form

$$F_m(U) = 0, \tag{35}$$

where the solution vector $U$ is comprised of all of the fields at all grid points, i.e.,

$$U = (\psi_0, \psi_1, \ldots, B^i_0, B^i_1, \ldots, (\alpha\Psi)_0, (\alpha\Psi)_1, \ldots, \phi_0, \phi_1, \ldots), \tag{36}$$

where the subscripts label the grid points. Note, however, that we also have to solve the algebraic equation (17), which is done in an iterative manner. We update $h$ and thus the matter distribution after the elliptic equations have been solved, and then the elliptic equations are solved again until we reach a certain tolerance. Because we have to iterate anyway, we do not solve the full system of equations (36), but rather solve the equations for $\psi$, $B^i$, $\alpha\Psi$, and $\phi$ individually one after the other within the overall iteration. Then the nonlinear system of equations we solve at once is

$$f_m(u) = 0, \tag{37}$$

where $u$ is now one of the six fields $\psi$, $B^i$, $\alpha\Psi$, or $\phi$. To find the solutions we use a Newton-Raphson scheme where $u$ is updated according to $u_{\rm new} = u_{\rm old} + x$ until a desired tolerance has been reached. As in any Newton scheme the correction $x$ is obtained by solving the linearized equations

$$\frac{\partial f_m(u)}{\partial u^n} x^n = -f_m(u). \tag{38}$$

The challenging part of the method is then to find an efficient way to solve this system of coupled linear equations. In the past [34,46–48], when using only six domains, we were able to use a direct solver for the sparse matrix $\frac{\partial f_m(u)}{\partial u^n}$. However, now that we are using 38 domains this is no longer efficient. We thus use an iterative generalized minimal residual (GMRES) solver. This solver needs a good preconditioner; otherwise, it will take too many iterations to find a solution to the linearized equations. A preconditioner is essentially an approximate inverse of the matrix $\frac{\partial f_m(u)}{\partial u^n}$ that can be computed efficiently. Here we use a block Jacobi method [76], i.e., we keep only certain blocks of the matrix $\frac{\partial f_m(u)}{\partial u^n}$ along the diagonal. Such a block-diagonal matrix $P$ is much easier to invert and thus $P^{-1}$ can be used as a preconditioner. We obtain these blocks by first dropping all entries in $\frac{\partial f_m(u)}{\partial u^n}$ that couple different computational domains. This results in 38 smaller blocks, each of which can be inverted more easily than the full matrix $\frac{\partial f_m(u)}{\partial u^n}$. To further speed up the computation of the preconditioner, we subdivide each box along both the $A$ and $B$ coordinate directions so that we end up with $2 \times 2 \times 38 = 152$ even smaller blocks along the diagonal of $P$, which can now be readily inverted by a direct solver for sparse matrices [77–81]. This block-diagonal inverse $P^{-1}$ is used as our preconditioner for the GMRES method, which allows us to solve the linear system in Eq. (38) so that we can take a Newton step.

Since we solve Eqs. (13), (14), (15), and (16) on 38 computational domains we need interdomain boundary conditions that connect them. In principle, these interdomain boundary conditions are very simple. One imposes that each field and its normal derivative are continuous across every interdomain boundary. These conditions are imposed by replacing the elliptic equation at each boundary point by either

$$u = u_{\rm adj} \tag{39}$$

or

$$n^i\partial_i u = n^i\partial_i u_{\rm adj}, \tag{40}$$

where $u_{\rm adj}$ is the field value in the adjacent domain, and $n^i$ is the vector normal to the boundary. Since both conditions have to be satisfied, one of them is imposed on the boundary points on one side of the boundary and the other is imposed on the other side in the adjacent domain. For the full system in Eq. (37) it does not matter which condition is used on which side. However, the preconditioner—which contains blocks that come from only one domain—is sensitive to this issue. It turns out that if one imposes the condition (40) on all sides of a domain, the block corresponding to this domain has a determinant of zero and thus cannot be inverted. In SGRID this problem is avoided by making sure that the condition (39) is imposed on at least one boundary of each domain. SGRID now has the ability to automatically find interdomain boundaries and impose consistent conditions on them.

### C. Modification to conformal factor equation

The conformal factor $\psi$ has to satisfy Eq. (13). Unfortunately, this equation is not guaranteed to have unique solutions. When this happens the linear solver fails and one cannot find initial data. We have observed that this does indeed happen when we try to construct initial data for very compact stars. The problem can easily be seen for zero shift ($B^i = 0$), where Eq. (13) takes the simple form

$$\bar{D}^2\psi = -2\pi\rho\psi^5. \tag{41}$$

If we linearize it we obtain

$$\bar{D}^2\delta\psi = -10\pi\rho\psi^4\delta\psi, \tag{42}$$

where $\delta\psi$ is the linearized conformal factor. Linear elliptic equations of this type are well known, and one can prove their uniqueness only if the coefficient in front of $\delta\psi$ on the right-hand side is positive (see, e.g., Ref. [82]). However, since both $\rho$ and $\psi$ are positive this coefficient is negative. One can fix this problem by introducing a rescaled density

$$\bar{\rho} = \psi^8\rho, \tag{43}$$

so that Eq. (13) becomes

$$\bar{D}^2\psi = -2\pi\bar{\rho}\psi^{-3} - \frac{\psi^5}{32\alpha^2}(\bar{L}B)^{ij}(\bar{L}B)_{ij}. \tag{44}$$

If we keep $\bar{\rho}$ constant while we solve this equation, its linearized version is

$$\bar{D}^2\delta\psi = +6\pi\bar{\rho}\psi^{-4}\delta\psi - \frac{5\psi^4}{32\alpha^2}(\bar{L}B)^{ij}(\bar{L}B)_{ij}\delta\psi, \tag{45}$$

which now is guaranteed to have unique solutions for $B^i = 0$. The downside of this approach is that instead of solving the equation once, one has to solve it iteratively. After each elliptic solve for $\psi$ one has to recompute $\bar{\rho}$ using Eq. (43), and then solve again until the changes in $\psi$ fall below a specified tolerance. However, as described below we have to solve our system of equations using an iterative approach anyway. We thus rescale $\rho$ according to Eq. (43) and only update $\bar{\rho}$ at the start of each overall iteration.

### D. Modification to velocity potential equation near the star surface

Notice that the elliptic equation (16) for the velocity potential $\phi$ reduces to a first-order equation at the star surface where $\rho_0 \to 0$. In fact, it reduces to Eq. (24) which we use as a boundary condition on the star surface. Nevertheless, in the star interior we solve Eq. (16). For challenging cases with high spins or high masses we find numerical problems close to the star surface arising from this equation. In these cases the first derivatives of $\phi$ can develop visible kinks just inside the star surface. These kinks tend to destabilize the overall iteration so that we cannot readily compute initial data. We have found that we can smooth out these kinks by replacing Eq. (16) with

$$\frac{c(\rho_0)\alpha}{h}\psi^{-4}\partial^2\phi + 2\frac{\rho_0\alpha}{h}\psi^{-5}(\partial_i\psi)(\partial_i\phi) + \left(D_i\frac{\rho_0\alpha}{h}\right)(D^i\phi) + D_i\left[\frac{\rho_0\alpha}{h}w^i - \rho_0\alpha u^0(\beta^i + \xi^i)\right] = 0. \tag{46}$$

In the first term we have added the function

$$c(\rho_0) = \rho_0 + \epsilon\rho_{0c}\left(\frac{\rho_{0c} - \rho_0}{\rho_{0c}}\right)^4, \tag{47}$$

which depends on a small number $\epsilon$ and on $\rho_{0c}$ which we choose to be equal to $\rho_0$ at the star center. For $\epsilon = 0$ we recover Eq. (16), but for positive $\epsilon$ the principal part of Eq. (46) now never vanishes. With this modification we are also able to find solutions in more challenging cases. We find that a value of $\epsilon = 0.1$ works for all cases we have considered. Consequently we consistently use this value, even though for lower spins or equal masses we can often use much lower values or even $\epsilon = 0$. While we have not yet tried a configuration with both very high spins and very high mass, we expect that $\epsilon = 0.1$ should work in these cases as well. Notice that $c(\rho_0) = \rho_0$ at the star center and that $c(\rho_0)$ differs from $\rho_0$ mostly near the star surface. Since at the star surface we impose the boundary condition (24) that is derived from the unmodified Eq. (16), the modifications to $\phi$ are small.

The neutron star surfaces always coincide with domain boundaries so that it is straightforward to impose the boundary condition (24) for $\phi$ at each star surface. Notice, however, that Eq. (16) and its boundary condition in Eq. (24) do not uniquely specify a solution $\phi$. If $\phi$ solves both Eqs. (16) and (24), $\phi + \text{const}$ will be a solution as well. In order to obtain a unique solution we demand that $\phi$

is zero at the star center, i.e., $\phi(x^i_{C*}) = 0$. We impose this condition by adding the term $\phi(x^i_{C*})$ to Eq. (46) on all grid points in the cubic domain covering the star center.

### E. Iteration scheme

The elliptic equations (44), (14), and (15) need to be solved in all domains, while the matter equations (46) and (17) are solved only inside each star. In order to solve the elliptic equations (44), (14), (15), and (46) we need a fixed domain decomposition. However, the location of the star surfaces (where $h = 1$) is not known *a priori*, but rather determined by Eq. (17). For this reason we use the following iterative procedure:

1. We first find an initial guess for $h$ within each star; in practice, we simply choose Tolman-Oppenheimer-Volkoff solutions (see, e.g., Chap. 23 in Ref. [83]) for each star. For the irrotational velocity potential we choose $\phi = \Omega(x^1_{C*} - x^1_{CM})x^2$, where $x^1_{C*}$ and $x^1_{CM}$ are the center of the star and the c.m. We choose the initial orbital angular velocity according to post-Newtonian theory.
2. If the residual of Eq. (46) is larger than 10% of the combined residuals of Eqs. (44), (14), and (15), we solve Eq. (46) for $\phi$. We then reset $\phi$ to $\phi = 0.2\phi_{\rm ell} + 0.8\phi_{\rm old}$, where $\phi_{\rm ell}$ is the just obtained solution of Eq. (46) and $\phi_{\rm old}$ is the previous value of $\phi$.
3. Next we solve the five coupled elliptic equations (44), (14), and (15) for $\Psi_{\rm ell} = (\psi, B^i, \alpha)_{\rm ell}$. We then set $\Psi = (\psi, B^i, \alpha)$ to $\Psi = 0.2\Psi_{\rm ell} + 0.8\Psi_{\rm old}$.
4. In order to solve Eq. (17) we need to know the values of the constants $C_\pm$ in each star as well as $\Omega$ and $x^1_{CM}$. We want to keep the star centers $x^1_{C*1/2}$ fixed at their initial position, so that the stars do not drift around during the iterations. The location of each star center is given by $\partial_1 h|_{x^1_{C*1/2}} = 0$. Note that this condition depends on $\Omega$ and $x^1_{CM}$. One strategy to find $\Omega$ and $x^1_{CM}$ is thus to use a root finder to adjust $\Omega$ and $x^1_{CM}$ until this condition is satisfied. This method is known as "force balance." In some cases we use this force balance method. However, it is often advantageous to fix $\Omega$ by other means, e.g., by using an eccentricity-reduction procedure as described in Appendix B. In this case one only needs to find $x^1_{CM}$. This can be achieved by adjusting $x^1_{CM}$ such that the $y$ component of the ADM linear momentum is zero. Here the $y$ direction denotes the direction perpendicular to both the orbital angular momentum and the line connecting the two star centers.
5. Next, we use Eq. (17) to update $h$ in each star, while at the same time adjusting $C_\pm$ such that the rest mass of each star remains constant. The domain boundaries need to be adjusted [by changing the surface functions such as $\sigma_1(A, B)$ in Eq. (28)] so that they remain at the star surfaces, which change whenever $h$ is updated.
6. We then evaluate the residuals [i.e., the $L^2$-norm of the left-hand sides of Eqs. (44), (14), (15), and (46)]. If the combined residual is below a prescribed tolerance we are done and exit the iteration at this point.
7. In order to ensure that the star centers always remain at their original position we use a root finder to find the locations where $\partial_i h = 0$. We then translate $h$ (and all other matter variables such as $\rho_0$ and $P$) by the amount necessary to bring them back to the original $x^1_{C*1/2}$.
8. Finally, we go back to step 2.

## IV. MASS, CENTER, MOMENTUM, AND SPIN OF INDIVIDUAL STARS

In general relativity no unambiguous definitions for the mass and spin of an individual star in a binary system exist. Here we introduce easy-to-compute estimates for such local quantities; see also, e.g., Refs. [29,45,84].

A star mass estimate can be obtained from

$$M \coloneqq -\frac{1}{2\pi}\int_* f^{kl}\partial_k\partial_l\psi\sqrt{f}d^3x. \tag{48}$$

This equation has the same form as the ADM mass for conformally flat metrics; however, the integration only runs over the star. Here $f_{ij} = \delta_{ij}$ is the flat conformal metric. We find that this quantity is much closer to the mass of an individual star with the same baryonic mass than an analog definition using the physical metric $\gamma_{ij} = \psi^4 f_{ij}$ in place of $f_{ij}$. Also, if one considers the special case of the Schwarzschild metric in conformally flat isotropic coordinates, the above definition yields the correct mass, while a definition using the physical metric $\gamma_{ij}$ would give a mass that is too large.

Since the above integral seems to capture the mass aspect of a star, we introduce an analogous integral to define the center of the star,

$$R^i_c \coloneqq -\frac{1}{2\pi}\int_* \frac{x^i - x^i_{CM}}{M} f^{kl}\partial_k\partial_l\psi\sqrt{f}d^3x. \tag{49}$$

This is essentially the same integral, except now weighted with the coordinate $x^i$ divided by the mass $M$.

In order to obtain a momentum estimate we start with

$$P(k) = \frac{1}{8\pi}\oint_* K_{ij}k^i n^j\sqrt{q}d^2y, \tag{50}$$

which is again inspired by the definitions for the ADM linear and angular momenta (see, e.g., Ref. [82]). However, the integration here only runs over the surface of the star.

Here, $n^i$ is the normal vector of the star surface and $q$ is the determinant of the metric induced on the surface by the physical metric and is given by

$$q_{ij} = \gamma_{ij} - n_i n_j, \qquad n_i = \gamma_{ij} n^j, \qquad n_i n^i = 1. \tag{51}$$

The vector $k^i$ is a symmetry vector that could be a translational or rotational Killing vector resulting in linear or angular momentum. However, since no exact Killing vectors will exist in the case of binaries, and also to keep things simple, we will construct $k^i$ from the coordinate unit vectors (1,0,0), (0,1,0), (0,0,1) for the case of linear momentum, and from the coordinate rotation vectors $(1,0,0)\times\vec{r}$, $(0,1,0)\times\vec{r}$, $(0,0,1)\times\vec{r}$, where $\vec{r} = (x,y,z)$. For linear momentum and angular momentum about $\vec{x}_{CM}$ we thus obtain

$$P^i \coloneqq \frac{1}{8\pi}\oint_* K_{il} n^l \sqrt{q} d^2 y \tag{52}$$

and

$$J^i \coloneqq \frac{1}{8\pi}\oint_* K_{kl} n^l \epsilon^{ijk} (x^j - x^j_{CM}) \sqrt{q} d^2 y. \tag{53}$$

Notice that we would obtain the same results for $P^i$ and $J^i$ if we had defined them using the conformal $\bar{K}_{ij} = \psi^2 K_{ij}$ while at the same time defining $q_{ij}$ to be the metric induced by the conformal metric $f_{ij}$. Also note that the usual surface integrals at infinity for ADM linear momentum and angular momentum can be converted into volume integrals. These volume integrals have support only within the stars, so that a natural definition for the star momentum is just this volume integral over the star. Furthermore, each such volume integral over the star can be rewritten in terms of a surface integral over the star surface. The expressions for the resulting surface integrals are the same as Eqs. (52) and (53). This means that for a binary the $J^i$ for each star will add up to the total ADM angular momentum. These facts should give us a measure of confidence in the definitions (52) and (53), probably more confidence than in the mass definition (48), where such arguments do not apply.

Now that we can compute the linear and angular momentum as well as the star center, we can define the star spin in the usual way as

$$S^i \coloneqq J^i - \epsilon^{ijk} R^j_c P^k. \tag{54}$$

The biggest uncertainty in this expression comes from $R^j_c$. However, since $R^j_c$ computed using Eqs. (48) and (49) is a ratio of integrals, errors in the mass definition may at least partially divide out.

## V. NUMERICAL RESULTS: INITIAL DATA CONSTRUCTION

### A. Initial data sequences

As a first test of the upgraded SGRID code, we compute initial data sequences for four sets of binary parameters, comparing the results of the old and new SGRID implementations (see also Appendix C). All configurations employ a piecewise-polytropic fit of the SLy EoS [34,74]. The gravitational masses are either $m_1 = m_2 = 1.375\ M_\odot$ with mass ratio $q = 1$, or $m_1 = 1.445\ M_\odot$, $m_2 = 1.156\ M_\odot$ with mass ratio $q = 1.25$, combined with the dimensionless spins $\chi = 0$ and $\chi = 0.05$. Figure 3 shows the ADM angular momenta ($J_{\mathrm{ADM}}$, top panel) and ADM masses ($M_{\mathrm{ADM}}$, bottom panel) as a functions of orbital velocity ($M\Omega$) for all four configurations and for the new and old SGRID code (dashed lines). The slight differences for large separations, i.e., small orbital frequencies, might be due to the different eccentricities of the individual setups.

In Fig. 4, we plot the binding energy

$$E_b = \frac{1}{\nu}\left(\frac{M_{\mathrm{ADM}}}{M} - 1\right) \tag{55}$$

versus the reduced orbital angular momentum

$$l = \frac{L}{\nu M^2} = \frac{J_{\mathrm{ADM}} - S_1 - S_2}{\nu M^2}. \tag{56}$$

Here $\nu = m_1 m_2 / M^2$ is the symmetric mass ratio, $M$ is the total mass, and $S_{1,2}$ are the individual spin magnitudes.

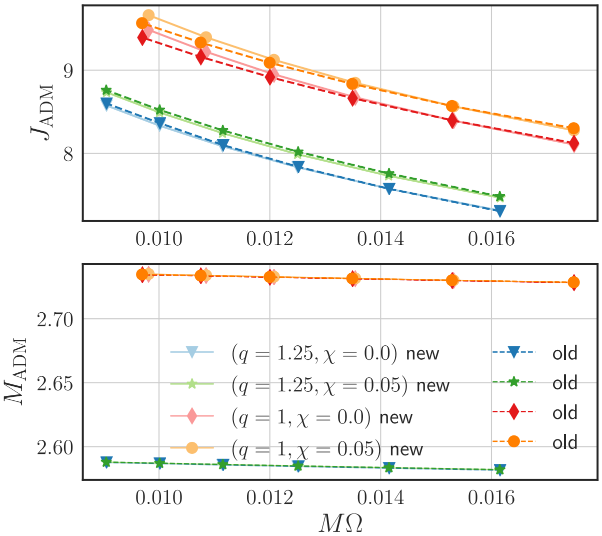

FIG. 3. ADM angular momentum ($J_{\mathrm{ADM}}$) and mass ($M_{\mathrm{ADM}}$) as a function of the angular orbital velocity $M\Omega$. Solid lines refer to results obtained with the new SGRID code, while dashed lines are those obtained with the old implementation.

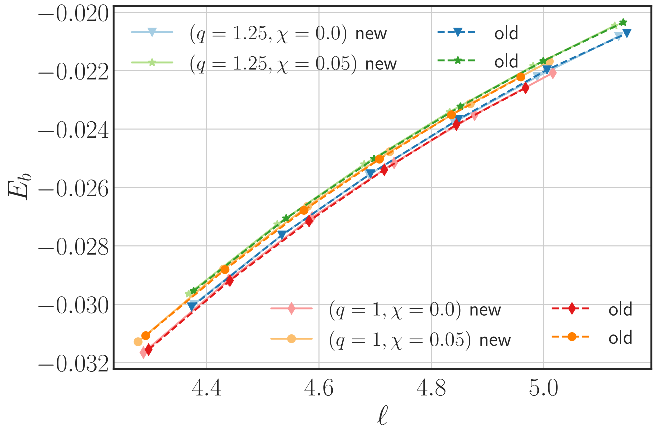

FIG. 4. Binding energy $E_b$ as a function of the reduced orbital angular momentum $\ell$ for different configurations, as discussed in the main text. Solid lines refer to results obtained with the new SGRID code, while dashed lines are those obtained with the old implementation.

In Fig. 4, the solid lines represent the new SGRID data while the dashed curves represent results obtained with the previous code version. We find that both results are in good agreement with each other, which validates our new implementation.

### B. Testing our spin definition for individual stars

In Table I we show the results of our mass and spin definitions [Eqs. (48) and (54)] for the case of a single star and a BNS system with and without spin. We see that the mass definition (48) for an individual star differs from the ADM mass in isolation (which is $m = 1.64$) by about 1% in the case of a binary, and is exact only for a single nonspinning star. The spin definition is exact for a single star and it is very likely that the spin estimates for binaries are better than 1% accurate [85], because of the partial cancellation of errors in $R^i_c$ discussed in Sec. IV.

In Fig. 5 we show the spin computed with Eq. (54) versus the spin angular velocity $\omega$ for an equal-mass binary with equal spins aligned with the orbital angular momentum. In this case we can reach a spin of $S/m^2 = 0.5763$ at $\omega = 0.0202$, which is slightly beyond the mass shedding limit of about 0.5705 for a single star with this polytropic equation of state [87]. If we further increase $\omega$, SGRID fails. This happens because during the iterations the star expands far into the domains that are supposed to be outside of the star such that it is impossible to adjust our domains to be surface fitting. We think that this is not a true failure of the program and should be expected to happen, since the stars will shed mass at these spin angular velocities.

TABLE I. Mass and spin estimates for the case of a polytropic equation of state $P = \kappa\rho_0^{1+1/n}$ with $\kappa = 123.6$, $n = 1$. For a binary with a separation of 47.2 (with $\Omega = 0.005096$), the mass definition differs from the ADM mass in isolation by about 1%. The spin definition is exact for a single star, and it is almost the same for a single star and a star in a binary if the spin angular velocity ($\omega = 0.01525$) is the same in both cases.

| $m_0 = 1.7745 \to$ TOV $m = 1.64$ | $M_1$ | $S_1$ | $S_1/m^2$ |
|---|---|---|---|
| one nonspinning star ($\omega = 0$) | 1.640 | 0 | 0 |
| one spinning star ($\omega = 0.01525$) | 1.646 | +0.8706 | +0.3237 |
| two nonspinning stars ($\omega = 0$) | 1.620 | −0.0007 | −0.0003 |
| two spinning stars ($\omega = 0.01525$) | 1.626 | +0.8652 | +0.3217 |

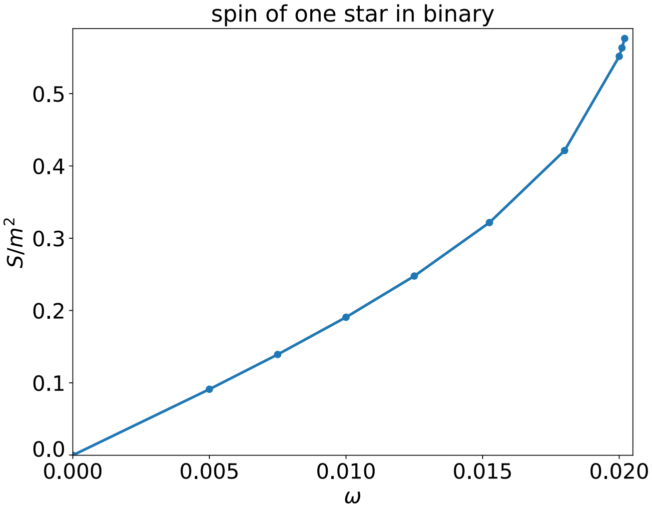

FIG. 5. Dimensionless spin of one star in an equal-mass binary with $m_{1/2} = 1.64$, $r_{12} = 47.2$, using a polytropic equation of state with $\kappa = 123.6$, $n = 1$.

## VI. NUMERICAL RESULTS: DYNAMICAL EVOLUTIONS

### A. Evolving millisecond pulsars

As discussed in the Introduction, NSs are expected to be spinning and a number of millisecond pulsars have been observed already (although none of them bound in a BNS system). To prove that our upgraded SGRID version is capable of simulating millisecond pulsars, we will present an equal-mass, aligned-spin configuration in which the individual baryonic masses of the two stars are $m^b_{1,2} = 1.494607$ and the rotational velocity (25) is set to $\omega_{1,2} = 0.03$.

We compute initial configurations for this system with two different SGRID resolutions, using $22 \times 22 \times 22$ and $26 \times 26 \times 26$ points in all domains. While the lower-resolution result for this challenging configuration can be computed in 52.4 hours, the higher-resolution run takes about 93.2 hours. Both initial data computations were performed on a single Intel Xeon node with 20 cores on FAU's Koko cluster. Due to the different resolutions, the initial configurations are slightly different, as shown in Table II. We find differences within the estimated masses of about 2% and dimensionless spins of about 3% between the quasilocal mass/spin measure (Sec. IV) and the single-star properties of a NS with the same EoS, baryonic mass, and

TABLE II. Mass and dimensionless spin for different resolutions for the binary millisecond configuration, as well as the ADM mass and angular momentum. The NS spin and mass estimates are computed from the quasilocal measures introduced before and from a comparison to single-star values estimated from isolated stars with the same EoS, baryonic mass, and rotational velocity as the individual constituents of the binary system.

| resolution | $m_{1,2}^{\text{quasiloc.}}$ | $\chi_{1,2}^{\text{quasiloc.}}$ | $m_{1,2}^{\text{singl.star}}$ | $\chi_{1,2}^{\text{signl.star}}$ | $M_{\text{ADM}}$ | $J_{\text{ADM}}$ |
|---|---|---|---|---|---|---|
| $22 \times 22 \times 22$ | 1.346800 | 0.59466 | 1.364748 | 0.57536 | 2.711566 | 9.8464958 |
| $26 \times 26 \times 26$ | 1.346948 | 0.59474 | 1.365494 | 0.57504 | 2.711535 | 9.8494049 |

rotational velocity. These differences show that the introduced quasilocal mass measure allows only an approximate extraction of the individual masses for binary configurations. For a high-quality analysis of high-resolution data, 2% differences in the individual masses (i.e., absolute differences of the order of $\sim 10^{-3}$) are well above the acceptable uncertainty of an analysis of the energetics of the system, for which uncertainties of $\sim 10^{-5}$ are typically required; see, e.g., Refs. [52,88,89]. We thus recommend using the ADM mass of a single star with the same baryonic mass and spin as the best available measure for the mass of an individual star. However, the situation is different for the introduced quasilocal spin measure. The fact that there is a 3% difference between the quasilocal spin of a star in a binary and the spin of a single star with the same EoS, baryonic mass, and rotational velocity does not mean that the quasilocal spin measure has a 3% error. Rather, it is quite likely that we are simply comparing two stars with different spins, because using the same rotational velocity ($\omega = 0.03$) does not necessarily lead to the same spin when we compare a star in a binary and a single star.

Despite these small differences, each case describes a binary in which both stars spin close to breakup. As far as we know, this is to date the highest spinning BNS simulation that includes the merger and postmerger. We evolve the system with the BAM code using 96 points within the finest refinement level. This resolution is not sufficient for a highly accurate GW signal needed for waveform model development, but sufficient to show that the simulation of binary millisecond systems is feasible. The NS tracks (for one star), the emitted GW signal, and the Hamiltonian constraint for the two resolutions are shown in Fig. 6. We find almost circular orbits with a residual eccentricity of $\sim 10^{-3}$, due to the employed eccentricity reduction. The difference between the phases of the GW signals shown in the middle panel of Fig. 6 is about 1 radian at the moment of merger. It is caused by (i) the different resolutions of the initial data, (ii) the slightly different masses of the configurations (cf. Table II), and (iii) the fact that eccentricity reduction was only applied to the low SGRID resolution, while we simply used the same values for $v_r$ and $\Omega$ for the high SGRID resolution. The bottom panel shows the Hamiltonian constraints, where we find only minor differences between the two SGRID resolutions.

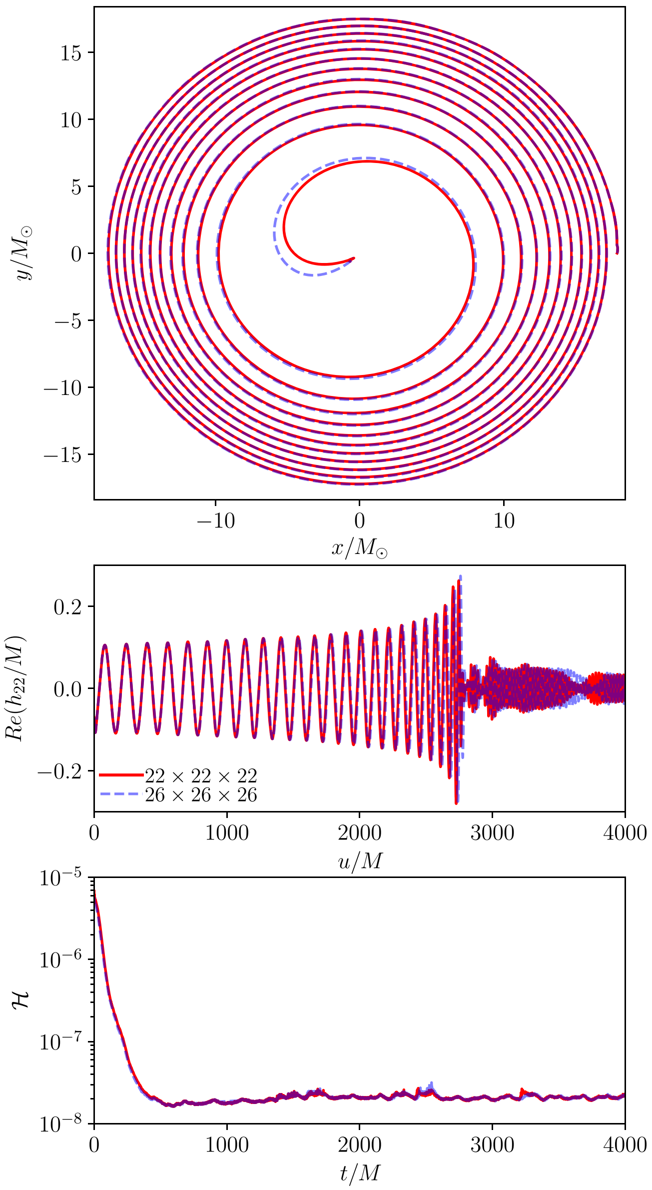

FIG. 6. NS tracks of a binary pulsar system as described in Table II for two different resolutions (top panel). We show the real part of the dominant (2,2) mode of the GW signal ($\text{Re}(h_{22})$) for both resolutions (middle panel) and the Hamiltonian constraint (bottom panel).

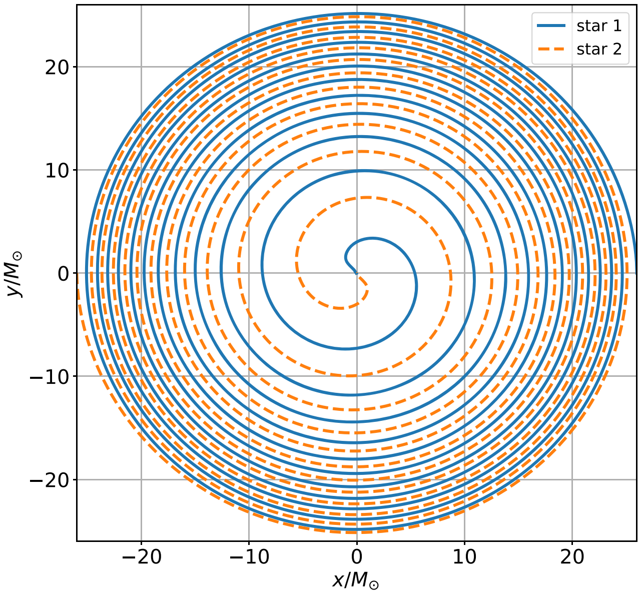

FIG. 7. Tracks of the star centers for the equal-mass binary with compactness $(\frac{m}{R})_\infty = 0.284$.

### B. Evolving highly compact stars

In the past we implemented the Hamiltonian constraint as in Eq. (13) and found that we were able to find a solution only for low compactness. With the modification given by Eq. (44) and described in Sec. III C we can now construct much more compact stars. As an example we have considered an equal-mass binary without spin, where each star has a baryonic mass of $m_0 = 2.4$ and obeys the SLy equation of state. This baryonic mass corresponds to a gravitational mass of $m = 2.0213$ and a compactness of $(\frac{m}{R})_\infty = 0.284$ for each star at infinite separation. The gravitational mass is thus very close to the maximum possible $m_{\text{max}} = 2.0606$ with the SLy equation of state. As far as we know, it is also the most compact BNS system evolved so far.

We have evolved this binary with BAM using a piecewise-polytropic fit for the SLy EoS [34,74] with an added thermal contribution to the pressure following a $\Gamma$ law with $\Gamma = 1.75$. In Fig. 7 we show the tracks of the two star centers starting from an initial coordinate separation of 52 up to merger. The initial orbital angular velocity and radial velocity are $\Omega = 0.0048738$ and $v_r = -0.00151$. The latter values have been obtained using the eccentricity-reduction procedure described in Appendix B.

### C. Evolving unequal-mass systems

In order to cover a larger set of configurations for binary neutron stars and to test the capability of the new version of SGRID, we have also constructed the initial data for a high-mass-ratio system. We chose the configuration to be composed of two nonspinning neutron stars with a piecewise-polytropic fit of the SLy EoS [34,74] with gravitational masses of 1.99 $M_\odot$ and 0.98 $M_\odot$, which results in a mass ratio of $q = 2.03$. This is the highest mass ratio considered for a soft equation of state in numerical relativity for a BNS system. While these mass ratios might even be at the edge of what is theoretically allowed, a study of these kinds of systems is essential to develop and improve waveform models; see, e.g., Ref. [62].

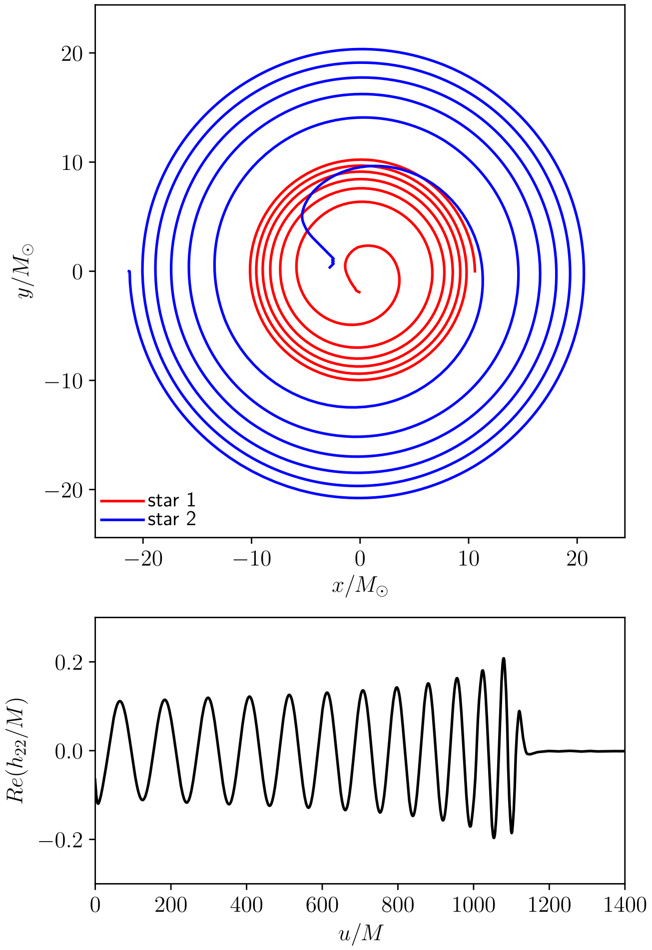

FIG. 8. NS tracks of the two stars in our high-mass-ratio simulation (top panel) and the real part of the dominant (2,2) mode of the GW signal (bottom panel).

In Fig. 8 we show the tracks of each neutron star in the binary after three steps of eccentricity reduction. These tracks illustrate the trajectory of the center of each neutron star in the $xy$ plane. The center of each neutron star is estimated as the minimum of the lapse inside each star. Near merger, the less massive star is disrupted, which causes the track of the less massive star to end.

In Fig. 8 we show the dominant (2,2) mode of the GW ($\text{Re}(h_{22})$) versus the retarded time. Due to the very large mass of the primary star the system undergoes a prompt collapse to a BH after the moment of merger. The gravitational-wave signal thus settles down very quickly after the merger.

## VII. SUMMARY

In this article we have presented upgrades made to the SGRID code to improve the capability of constructing initial data for numerical relativity simulations. Among other things, our upgrades involve a new grid structure, the use of different coordinates, as well as a reformulation of the equations for the conformal factor and the velocity potential. In order to compare with other methods or models such as post-Newtonian theory, one would like to know certain physical quantities such as the mass and spin of each star. We have presented simple estimates for the initial mass, spin, momentum, and c.m. of each individual star.

We have tested our new implementation by comparing results against the previous SGRID version and found good agreement between initial data sequences. We also observed lower constraint violations (see Appendix C), and in addition were able to construct more demanding initial data sets with high spins, masses, and mass ratios.

To show that the new code version will be of importance within the field of numerical relativity, we have constructed initial data for a binary system with individual stars close to the breakup and to the maximum mass allowed by the equation of state, as well as a BNS system with a soft equation of state characterized by a high mass ratio of $q = 2.03$. All of these simulations enter previously unexplored regions of the BNS parameter space. Due to an eccentricity-reduction procedure, the presented simulations have typical eccentricities of $\sim 10^{-3}$. This allows them to be used for the calibration and validation of gravitational waveform models.

In the future, we plan to use SGRID's new capabilities to perform new simulations and extend the publicly available CoRe database [65] with high-quality data, which was previously not accessible within the numerical relativity community.

## ACKNOWLEDGMENTS

It is a pleasure to thank Sebastiano Bernuzzi, Erik Lundberg, and Jason Mireles-James for helpful discussions. This work was supported by NSF Grant No. PHY-1707227 and DFG Grant No. BR 2176/5-1. T. D. acknowledges support by the European Union's Horizon 2020 research and innovation program under Grant Agreement No. 749145, BNSmergers. We also acknowledge usage of computer time on the HPC cluster KOKO at Florida Atlantic University, on the Minerva cluster at the Max Planck Institute for Gravitational Physics, on SuperMUC at the LRZ (Munich) under the project number pn56zo, and on the ARA cluster of the University of Jena.

## APPENDIX A: EMPIRICAL $\omega$-$\chi$ RELATION

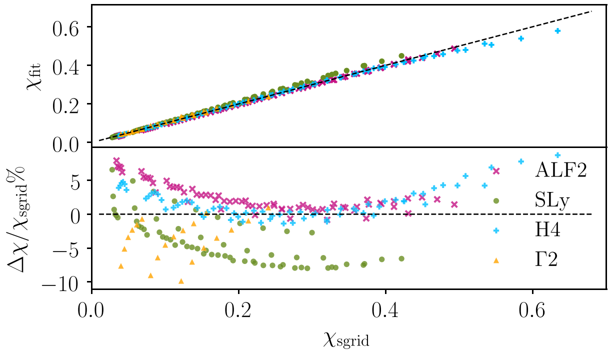

FIG. 9. The dimensionless spin according to Eq. (A1) as a function of spin computed in the new SGRID for different EoSs (top panel). The fractional residuals are shown in the bottom panel. The black dashed curve represents the $\chi_{\rm SGRID} = \chi_{\rm fit}$ scenario.

As shown, SGRID can construct initial configurations in which the individual stars have arbitrary spin [34,46,47]. However, for this one has to specify the angular velocity of the fluid $\omega$, the baryonic masses, and the EoS as input parameters. The spin itself cannot be specified directly. Thus, to minimize computational costs and simplify the computation, we need to find an ansatz for the spin in terms of SGRID's input parameter. One such phenomenological fit has been given in Appendix C.2 of Ref. [34]. However, we found that it might give large errors at high spins, which are now reachable with our new SGRID implementation. Therefore, building upon that, we fit the following data generated for a single star to the SGRID output for $\chi_{\rm SGRID}$. We use four EoSs (SLy, ALF2, H4, and a $\Gamma = 2$ polytrope) with baryonic masses $M_b/M_\odot \in [1.1, 1.7]$ in steps of 0.1 and compactnesses in the range $\mathcal{C} \in [0.09, 0.20]$. We find the following phenomenological fit for the dimensionless spin magnitude $\chi$ of a single NS:

$$\chi_{\rm fit} = a_1(1 + m_1 M_b)(1 + c_1\mathcal{C} + c_2\mathcal{C}^2 + c_3\mathcal{C}^3 + c_4\mathcal{C}^4) \times (1 + d_1\omega)\omega, \tag{A1}$$

where the coefficients $a_1 = 59.329$, $m_1 = 1.9267$, $c_1 = -17.1537$, $c_2 = 122.8986$, $c_3 = -401.3542$, $c_4 = 483.0869$, and $d_1 = 10.2497$ are computed by fitting the data, cf. Fig. 9. Specifically, for all combinations of NS mass and EoS we employ ten different values of $\omega \in [0.000, 0.02]$ in steps of $\Delta\omega = 0.002$. The fractional residuals for each configuration are shown in the bottom panel Fig. 9. The new fit gives a maximum error of 10% for some extreme cases; otherwise, the error is below 5%.

## APPENDIX B: Ω-BASED ECCENTRICITY-REDUCTION PROCEDURE

In most cases we have used an eccentricity-reduction procedure very similar to the one in Ref. [45], instead of the one described in Ref. [34], because in many cases it is advantageous to avoid using the "force balance" relation mentioned in point 4 of Sec. III E.

We start with a post-Newtonian estimate for $\Omega$ as well as $v_r = 0$. We then evolve for about three orbits and fit the observed distance $d(t)$ between the star centers to

$$S(t) = S_0 + A_0 t + \frac{A_1}{2} t^2 - \frac{B}{\omega_f} \cos(\omega_f t + \phi), \qquad \text{(B1)}$$

where $S_0, A_0, A_1, B, \omega_f$, and $\phi$ are fit parameters. From the fit parameters we compute the measured eccentricity

$$e = -\frac{B}{\omega_f d_0} \qquad \text{(B2)}$$

as well as the changes

$$\delta v_r = -B \sin\phi, \qquad \delta\Omega = -\frac{B \omega_f \cos\phi}{2\Omega d_0} \qquad \text{(B3)}$$

in $v_r$ and $\Omega$ needed to lower the eccentricity. We then recompute initial data with the new values for $v_r$ and $\Omega$, and evolve and fit again to obtain the next set of changes to $v_r$ and $\Omega$. We usually perform three or four such reduction steps. Notice that we typically use the proper distance as the distance measure $d(t)$ that we fit, and that we set $d_0$ equal to the initial coordinate distance. The latter has given slightly better estimates for $\delta v_r$ and $\delta\Omega$ than simply setting $d_0 = S_0$.

## APPENDIX C: COMPARISON WITH THE OLD VERSION OF SGRID

In order to test the new implementation, we have constructed and evolved initial data with the same physical parameters using the two different SGRID versions. We use the same configuration for both initial data, namely, a $\Gamma = 2$, $\kappa = 123.6489$ EoS. The system is an equal-mass binary in which the individual stars have a baryonic mass of $1.625\ M_\odot$. The initial separation between the stars is 68.8 km.

Figure 10 shows the Hamiltonian constraint across one of the stars at the initial time after interpolating the SGRID data onto BAM's grid. As we can see, the new SGRID version (solid line) produces smaller constraint violations than the old version (broken line) inside the star, while at the star surfaces both lead to approximately the same violations. Outside the stars, the old SGRID version seems slightly superior.

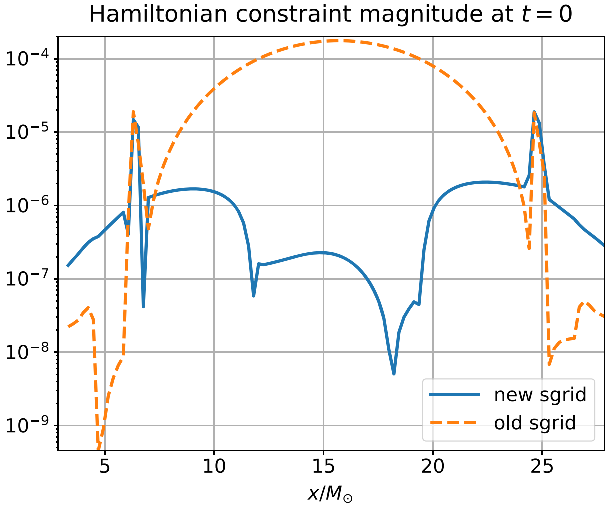

FIG. 10. The Hamiltonian constraint across one of the stars at the initial time for both the old (broken line) and new (solid line) version of SGRID. Similar violations occur in both approaches near the star surfaces, but inside the stars the new version shows less violations.

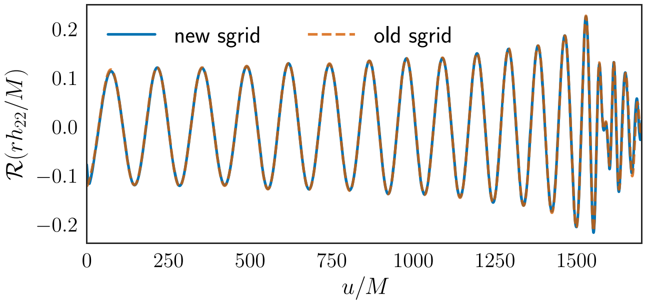

FIG. 11. Comparison between the GW signals computed for the same physical configurations computed with the old and new SGRID code. Old SGRID results are shown by the orange dashed curve, while new SGRID results are shown by the blue solid curve.

In Fig. 11 we show the dominant (2,2) mode of GW. We evolve both initial data sets with BAM using exactly the same setup for both evolutions, namely, six refinement levels and 96 points to cover the star. The GWs are extracted at a distance of $900\ M_\odot$. Waveforms are aligned for the two cases at early times, i.e., before $u \leq 600M$. We find that both waves agree very well throughout the merger and in the early postmerger part; see Fig. 11.

---

[1] While also other sources such as a black hole-neutron star mergers [2–4] or even exotic scenarios like axion star-neutron star mergers [5] could explain the observed GW signal and a bright electromagnetic counterpart, the observation of a blue kilonova signature several hours up to a day after the merger disfavors in part a black hole-neutron star progenitor system (see, e.g., [6]), which makes a BNS the most likely source for GW170817.

[2] H. Yang, W. E. East, and L. Lehner, Astrophys. J. **856**, 110 (2018); **870**, 139(E) (2019).
[3] T. Hinderer *et al.*, Phys. Rev. D **100**, 063021 (2019).
[4] M. W. Coughlin and T. Dietrich, Phys. Rev. D **100**, 043011 (2019).
[5] T. Dietrich, F. Day, K. Clough, M. Coughlin, and J. Niemeyer, Mon. Not. R. Astron. Soc. **483**, 908 (2019).
[6] D. M. Siegel, Eur. Phys. J. A **55**, 203 (2019).
[7] B. P. Abbott *et al.* (LIGO Scientific and Virgo Collaboration), Phys. Rev. Lett. **119**, 161101 (2017).
[8] B. P. Abbott *et al.* (LIGO Scientific, Virgo, Fermi GBM, INTEGRAL, IceCube, AstroSat Cadmium Zinc Telluride Imager Team, IPN, Insight-Hxmt, ANTARES, Swift, AGILE Team, 1M2H Team, Dark Energy Camera GW-EM, DES, DLT40, GRAWITA, Fermi-LAT, ATCA, ASKAP, Las Cumbres Observatory Group, OzGrav, DWF (Deeper Wider Faster Program), AST3, CAASTRO, VINROUGE, MASTER, J-GEM, GROWTH, JAGWAR, CaltechNRAO, TTU-NRAO, NuSTAR, Pan-STARRS, MAXI Team, TZAC Consortium, KU, Nordic Optical Telescope, ePESSTO, GROND, Texas Tech University, SALT Group, TOROS, BOOTES, MWA, CALET, IKI-GW Follow-up, H.E.S.S., LOFAR, LWA, HAWC, Pierre Auger, ALMA, Euro VLBI Team, Pi of Sky, Chandra Team at McGill University, DFN, ATLAS Telescopes, High Time Resolution Universe Survey, RIMAS, RATIR, and SKA South Africa/MeerKAT Collaborations), Astrophys. J. **848**, L12 (2017), 1710.05833.
[9] G. B. Cook, Living Rev. Relativity **3**, 5 (2000).
[10] W. Tichy, Rep. Prog. Phys. **80**, 026901 (2017).
[11] R. Haas *et al.*, Phys. Rev. D **93**, 124062 (2016).
[12] M. Favata, Phys. Rev. Lett. **112**, 101101 (2014).
[13] M. Agathos, J. Meidam, W. Del Pozzo, T. G. F. Li, M. Tompitak, J. Veitch, S. Vitale, and C. V. D. Broeck, Phys. Rev. D **92**, 023012 (2015).
[14] A. Samajdar and T. Dietrich, Phys. Rev. D **100**, 024046 (2019).
[15] J. W. T. Hessels, S. M. Ransom, I. H. Stairs, P. C. C. Freire, V. M. Kaspi, and F. Camilo, Science **311**, 1901 (2006).
[16] R. S. Lynch, P. C. C. Freire, S. M. Ransom, and B. A. Jacoby, Astrophys. J. **745**, 109 (2012).
[17] K. Stovall *et al.*, Astrophys. J. **854**, L22 (2018).
[18] H. T. Cromartie *et al.*, arXiv:1904.06759.
[19] T. Dietrich and M. Ujevic, Classical Quantum Gravity **34**, 105014 (2017).
[20] M. W. Coughlin, T. Dietrich, S. Antier, M. Bulla, F. Foucart, K. Hotokezaka, G. Raaijmakers, T. Hinderer, and S. Nissanke, arXiv:1910.11246.
[21] B. P. Abbott *et al.* (LIGO Scientific and Virgo Collaborations), Phys. Rev. X **9**, 011001 (2019).
[22] A. Chen, N. K. Johnson-McDaniel, T. Dietrich, and R. Dudi, to be published.
[23] A. Bauswein, T. W. Baumgarte, and H. T. Janka, Phys. Rev. Lett. **111**, 131101 (2013).
[24] S. Köppel, L. Bovard, and L. Rezzolla, Astrophys. J. **872**, L16 (2019).
[25] V. Paschalidis and M. Ruiz, Phys. Rev. D **100**, 043001 (2019).
[26] C. Palenzuela, L. Lehner, M. Ponce, S. L. Liebling, M. Anderson, D. Neilsen, and P. Motl, Phys. Rev. Lett. **111**, 061105 (2013).
[27] C. Mills, V. Tiwari, and S. Fairhurst, Phys. Rev. D **97**, 104064 (2018).
[28] T. Hinderer, B. D. Lackey, R. N. Lang, and J. S. Read, Phys. Rev. D **81**, 123016 (2010).
[29] T. Dietrich, S. Bernuzzi, M. Ujevic, and W. Tichy, Phys. Rev. D **95**, 044045 (2017).
[30] L. Lehner, S. L. Liebling, C. Palenzuela, O. L. Caballero, E. O'Connor, M. Anderson, and D. Neilsen, Classical Quantum Gravity **33**, 184002 (2016).
[31] F. Zappa, S. Bernuzzi, D. Radice, A. Perego, and T. Dietrich, Phys. Rev. Lett. **120**, 111101 (2018).
[32] K. Kiuchi, K. Kyutoku, M. Shibata, and K. Taniguchi, Astrophys. J. **876**, L31 (2019).
[33] M. Dominik, K. Belczynski, C. Fryer, D. E. Holz, E. Berti, T. Bulik, I. Mandel, and R. O'Shaughnessy, Astrophys. J. **759**, 52 (2012).
[34] T. Dietrich, N. Moldenhauer, N. K. Johnson-McDaniel, S. Bernuzzi, C. M. Markakis, B. Brügmann, and W. Tichy, Phys. Rev. D **92**, 124007 (2015).
[35] J. G. Martinez, K. Stovall, P. C. C. Freire, J. S. Deneva, F. A. Jenet, M. A. McLaughlin, M. Bagchi, S. D. Bates, and A. Ridolfi, Astrophys. J. **812**, 143 (2015).
[36] P. Lazarus *et al.*, Astrophys. J. **831**, 150 (2016).
[37] LORENE: Langage Objet pour la RElativité NumériquE, http://www.lorene.obspm.fr.
[38] K. Kyutoku, M. Shibata, and K. Taniguchi, Phys. Rev. D **90**, 064006 (2014).
[39] W. E. East, F. M. Ramazanoglu, and F. Pretorius, Phys. Rev. D **86**, 104053 (2012).
[40] N. Moldenhauer, C. M. Markakis, N. K. Johnson-McDaniel, W. Tichy, and B. Brügmann, Phys. Rev. D **90**, 084043 (2014).
[41] T. Dietrich, S. Ossokine, and K. Clough, Classical Quantum Gravity **36**, 025002 (2019).
[42] A. Tsokaros and K. Uryu, J. Eng. Math. **82**, 1 (2012).
[43] A. Tsokaros, K. Uryu, and L. Rezzolla, Phys. Rev. D **91**, 104030 (2015).
[44] F. Foucart, L. E. Kidder, H. P. Pfeiffer, and S. A. Teukolsky, Phys. Rev. D **77**, 124051 (2008).
[45] N. Tacik *et al.*, Phys. Rev. D **92**, 124012 (2015).
[46] W. Tichy, Phys. Rev. D **74**, 084005 (2006).
[47] W. Tichy, Classical Quantum Gravity **26**, 175018 (2009).
[48] W. Tichy, Phys. Rev. D **80**, 104034 (2009).
[49] H. R. Rüter, D. Hilditch, M. Bugner, and B. Brügmann, Phys. Rev. D **98**, 084044 (2018).
[50] T. Vincent, H. P. Pfeiffer, and N. L. Fischer, Phys. Rev. D **100**, 084052 (2019).
[51] We refer here solely to simulations based on consistent initial data, where *consistent* refers to simultaneously solving the Einstein equations and the equations of general relativistic hydrodynamics.
[52] S. Bernuzzi, T. Dietrich, W. Tichy, and B. Brügmann, Phys. Rev. D **89**, 104021 (2014).
[53] T. Dietrich, S. Bernuzzi, B. Brügmann, and W. Tichy, in *Proceedings, 26th Euromicro International Conference on Parallel, Distributed and Network-Based Processing (PDP 2018): Cambridge, UK* (2018), pp. 682–689, https://doi.org/10.1109/PDP2018.2018.00113.
[54] E. R. Most, L. J. Papenfort, A. Tsokaros, and L. Rezzolla, Astrophys. J. **884**, 40 (2019).

[55] A. Tsokaros, M. Ruiz, V. Paschalidis, S. L. Shapiro, and K. Uryu, Phys. Rev. D **100**, 024061 (2019).

[56] W. E. East, V. Paschalidis, F. Pretorius, and A. Tsokaros, arXiv:1906.05288.

[57] T. Dietrich, S. Bernuzzi, B. Brügmann, M. Ujevic, and W. Tichy, Phys. Rev. D **97**, 064002 (2018).

[58] F. Foucart, R. Haas, M. D. Duez, E. O'Connor, C. D. Ott, L. Roberts, L. E. Kidder, J. Lippuner, H. P. Pfeiffer, and M. A. Scheel, Phys. Rev. D **93**, 044019 (2016).

[59] K. Kiuchi, K. Kawaguchi, K. Kyutoku, Y. Sekiguchi, M. Shibata, and K. Taniguchi, Phys. Rev. D **96**, 084060 (2017).

[60] T. Dietrich, S. Bernuzzi, and W. Tichy, Phys. Rev. D **96**, 121501 (2017).

[61] F. Foucart *et al.*, Phys. Rev. D **99**, 044008 (2019).

[62] T. Dietrich, A. Samajdar, S. Khan, N. K. Johnson-McDaniel, R. Dudi, and W. Tichy, Phys. Rev. D **100**, 044003 (2019).

[63] K. Kiuchi, K. Kyohei, K. Kyutoku, Y. Sekiguchi, and M. Shibata, arXiv:1907.03790.

[64] S. V. Chaurasia, T. Dietrich, N. K. Johnson-McDaniel, M. Ujevic, W. Tichy, and B. Brügmann, Phys. Rev. D **98**, 104005 (2018).

[65] T. Dietrich, D. Radice, S. Bernuzzi, F. Zappa, A. Perego, B. Brügmann, S. V. Chaurasia, R. Dudi, W. Tichy, and M. Ujevic, Classical Quantum Gravity **35**, 24LT01 (2018).

[66] D. Radice, A. Perego, K. Hotokezaka, S. A. Fromm, S. Bernuzzi, and L. F. Roberts, Astrophys. J. **869**, 130 (2018).

[67] T. Dietrich, M. Ujevic, W. Tichy, S. Bernuzzi, and B. Brügmann, Phys. Rev. D **95**, 024029 (2017).

[68] B. P. Abbott *et al.* (Virgo and LIGO Scientific Collaborations), Phys. Rev. Lett. **121**, 161101 (2018).

[69] B. P. Abbott *et al.* (LIGO Scientific and Virgo Collaborations), Phys. Rev. Lett. **123**, 011102 (2019).

[70] W. Tichy, Phys. Rev. D **84**, 024041 (2011).

[71] W. Tichy, Phys. Rev. D **86**, 064024 (2012).

[72] H. Rüter, Ph.D. thesis, Friedrich-Schiller-Universität Jena, 2019, https://www.db-thueringen.de/receive/dbt_mods_00039088.

[73] R. Arnowitt, S. Deser, and C. W. Misner, in *Gravitation: An Introduction to Current Research*, edited by L. Witten (John Wiley, New York, 1962), pp. 227–265.

[74] J. S. Read, B. D. Lackey, B. J. Owen, and J. L. Friedman, Phys. Rev. D **79**, 124032 (2009).

[75] M. Ansorg, Classical Quantum Gravity **24**, S1 (2007).

[76] G. Reifenberger, Ph.D. thesis, Florida Atlantic University, 2013.

[77] T. A. Davis and I. S. Duff, SIAM J. Matrix Anal. Appl. **18**, 140 (1997).

[78] T. A. Davis and I. S. Duff, ACM Trans. Math. Softw. **25**, 1 (1999).

[79] T. A. Davis, ACM Trans. Math. Softw. **30**, 196 (2004).

[80] T. A. Davis, ACM Trans. Math. Softw. **30**, 165 (2004).

[81] T. A. Davis, UMFPACK a sparse linear systems solver using the Unsymmetric MultiFrontal method, http://www.cise.ufl.edu/research/sparse/umfpack/.

[82] E. Gourgoulhon, arXiv:gr-qc/0703035.

[83] C. W. Misner, K. S. Thorne, and J. A. Wheeler, *Gravitation* (W. H. Freeman, San Francisco, 1973).

[84] M. Campanelli, C. O. Lousto, Y. Zlochower, B. Krishnan, and D. Merritt, Phys. Rev. D **75**, 064030 (2007).

[85] As we can see $S_1$ is not exactly zero for $\omega = 0$ in the case of binaries. In Eq. (F10) of [86] it is demonstrated that one may expect a nonzero spin angular velocity $\Omega_s$ even for irrotational stars. However, our initial data formulation as well as our new spin definition differ from the approach in [86]. To compare we can estimate the moment of inertia as $I \sim S_1/\omega \sim 50$ from the slope of Fig. 5. So $S_1 = -0.0007$ corresponds to $\Omega_s = S_1/I = -1.5 \times 10^{-5}$ and thus $\Omega_s/\Omega = -0.003$, which is much smaller than the 0.06 predicted by Eq. (F10) of [86].

[86] P. Marronetti and S. L. Shapiro, Phys. Rev. D **68**, 104024 (2003).

[87] M. Ansorg, A. Kleinwächter, and R. Meinel, Astron. Astrophys. **405**, 711 (2003).

[88] T. Damour, A. Nagar, D. Pollney, and C. Reisswig, Phys. Rev. Lett. **108**, 131101 (2012).

[89] T. Dietrich and T. Hinderer, Phys. Rev. D **95**, 124006 (2017).